Goal-oriented error estimation and mesh adaptivity in 3d elastoplasticity problems

2 authors:

Some of the authors of this publication are also working on these related projects:

HORIZON 2020: Environmentally best practices and optmisation in hydraulic fracturing for shale gas/oil development   View project

Mathematical Analysis and Numerical Simulation of Bioabsorbable Stents   View project

Goal-Oriented Error Estimation and Mesh Adaptivity in 3d Elastoplasticity Problems

S.Sh. Ghorashi[a,*], T. Rabczuk[b,c,*]

[a]*Research Training Group 1462, Bauhaus-Universität Weimar, Weimar, Germany*
[b]*Division of Computational Mechanics, Ton Duc Thang University, Ho Chi Minh City, Vietnam*
[c]*Institute of Structural Mechanics, Bauhaus-Universität Weimar, Weimar, Germany*

Abstract

We propose a 3D adaptive method for plasticity problems based on goal-oriented error estimation, which computes the error with respect to a prescribed quantity of interest. It is a dual-based scheme which requires an adjoint problem. The computed element-wise errors at each load/displacement increment are utilized for the mesh adaptivity purpose. Mesh adaptivity procedure is performed based on refinement and coarsening by introducing hanging nodes in quadrilateral and hexahedral elements in 2d and 3d, respectively. Several numerical simulations are investigated and the results are compared with available analytical solutions, existing experimental data and results of mesh adaptivity based on other conventional error estimation methods.

Keywords: Goal-Oriented Error Estimation, Mesh Adaptivity, Elastoplasticity, Von-Mises Stress

1. INTRODUCTION

Three-dimensional simulation of elastoplastic material plays a significant role in the analysis and design of numerous engineering applications, e.g. prediction of ductile failure. Since it is a nonlinear problem, its computational cost is notably increased by uniformly refining the mesh to achieve highly accurate results. Accordingly, mesh adaptation would be a profitable tool to reduce the computational burden.

Nowadays, many challenging engineering problems are solved by numerical simulations. The Finite Element Method (FEM) is one of the most popular numerical approach. Albeit, many other computational approaches such as meshfree methods [1–5], extended finite element method [6] and extended isoge-

---

*Corresponding authors
Email addresses: `shahram.ghorashi@uni-weimar.de` (S.Sh. Ghorashi),
`timon.rabczuk@tdt.edu.vn` (T. Rabczuk)

ometric analysis method [7–10] have been spececifically developed for fracture modeling, FEM is still most widely used in engineering analyses and design.

Adaptive methods can be categorized into three different classes: h-, r- and p-adaptivity. In h-adaptivity the discretization is refined while p-adaptivity refers to locally increasing the polynomial order of the shape functions. R-adaptivity aims to find the optimal mesh topology for a given discretization. P-adaptivity is not well suited for problems involving localized deformation and plasticity since high gradients and localized deformation cannot be captured well with higher order. In this contribution, we consider h-adaptivity where the mesh is refined and coarsened based on the estimated element-wise errors.

There exist different types of discretization error estimates, including residual-based [11] and recovery-based [12] error estimations. While a residual-based error estimator utilizes the residuals of a governing differential equation and its boundary conditions as an error criterion, recovery-based methods [13, 14] utilize the gradient of solutions. The conventional error estimation methods approximate errors in the energy norm. However, in many engineering applications other quantities are of major interest, e.g. the displacement at a point, mean stress in a region, load-deflection curve etc. In such cases error estimators for the energy norm are not appropriate tools to estimate the error of a individual quantity, or to achieve an efficient mesh to solve it accurately. Therefore, the so-called goal-oriented error estimation (GOEE) methods based on duality techniques have been developed to estimate the error in specific quantities of interest [15–24]. One of the most well-known techniques of goal-oriented error estimation is the Dual-Weighted Residual (DWR) method introduced in [15]. It is a weighted form of the residual-based error estimator where the weights are calculated by solving a dual/adjoint problem. Rannacher and Suttmeier have developed and applied the DWR error estimation to two-dimensional linear elasticity and elastic perfect plasticity problems [25–27]. Suttmeier extended his work later to plasticity with hardening and solved a 2d test example [28]. Ghorashi et al. applied the DWR-based Goal-oriented mesh adaptivity approach to 2d elasticity problems with heterogeneous material distribution [29] and 3d elasticity problems [30].

In this contribution, the Dual-Weighted Residual error estimation is extended to three-dimensional elastoplasticity problems with linear isotropic hardening. Local estimated errors are exploited in order to accomplish the local mesh adaptivity. The goal-oriented mesh adaptivity controls the local errors in terms of the prescribed quantity. This 3d elastoplasticity FEM simulation accompanying the goal-oriented mesh adaptivity has been implemented in C++ programming language within the framework of the opensource FEM library, deal.II [31, 32].

Several numerical simulations are performed and the results are compared with available analytical solutions, existing experimental data and the results of mesh adaptivity based on other typical error estimation methods.

The remainder of the paper is structured as follows: Section 2 describes the elastoplasticity problem with linear isotropic hardening. The goal-oriented error estimation is presented in Section 3. Section 4 depicts the goal-oriented

mesh adaptivity procedure. In Section 5, numerical investigations are provided. Finally, concluding remarks are outlined in Section 6.

2. ELASTOPLASTICITY PROBLEM

2.1. Governing equations

In the following, the governing equations for computing the displacement field $\mathbf{u} \in \mathbf{V} := \{\mathbf{v} \in [H^1(\Omega)]^d\}$, stress tensor $\boldsymbol{\sigma}$ and plastic strain tensor $\boldsymbol{\varepsilon}^p$ in a domain $\Omega \subset \mathbb{R}^d$ (d denotes the dimension size) are described.

- Equilibrium equation:

$$-\nabla \cdot \boldsymbol{\sigma} = \mathbf{f}, \quad \text{in } \Omega. \tag{1}$$

- Constitutive relationship: Relationship between strain $\boldsymbol{\varepsilon}(\mathbf{u}) = \frac{1}{2}\left(\nabla\mathbf{u} + (\nabla\mathbf{u})^T\right)$ and stress σ:

$$\boldsymbol{\sigma} = \mathbb{C}^e : (\boldsymbol{\varepsilon}(\mathbf{u}) - \boldsymbol{\varepsilon}^p), \tag{2}$$

where $\mathbb{C}^e$ is the fourth-order material property tensor in the elastic case.

- Complementarity condition:

$$\dot{\boldsymbol{\varepsilon}}^p : (\boldsymbol{\tau} - \boldsymbol{\sigma}) \geq 0, \quad \forall \boldsymbol{\tau} \text{ with } F(\boldsymbol{\tau}, \sigma_y) \leq 0. \tag{3}$$

where τ is in the admissible stress space and $\dot{\boldsymbol{\varepsilon}}^p$ is the strain increment; σ_y denotes the yield stress. Note that $\dot{\boldsymbol{\varepsilon}}^p = 0$ if $F(\boldsymbol{\sigma}, \sigma_y) < 0$ and $\dot{\boldsymbol{\varepsilon}}^p$ may be a nonzero tensor if and only if $F(\boldsymbol{\sigma}, \sigma_y) = 0$. The above complementarity condition can be reformulated as equality using the Chen-Mangasarian replacement functions [33–35].

- Essential boundary condition:

$$\mathbf{u} = \bar{\mathbf{u}}, \quad \text{on } \Gamma_d. \tag{4}$$

- Natural (Neumann) boundary condition:

$$\boldsymbol{\sigma} \cdot \mathbf{n} = \bar{\mathbf{t}}, \quad \text{on } \Gamma_n. \tag{5}$$

where $\bar{\mathbf{u}}$ and $\bar{\mathbf{t}}$ are prescribed displacement and traction imposed on the boundaries Γ_d and Γ_n, respecively.

The internal stresses $\boldsymbol{\sigma}(\mathbf{x})$ are restricted to some maximal stress, i.e. that fulfills an inequality $F(\boldsymbol{\sigma}, \sigma_y) \leq 0$ at every point $\mathbf{x}$. An example of such a function is the von Mises flow function $F(\boldsymbol{\sigma}, \sigma_y) = \sigma_v - \sigma_y$ where

$$\sigma_v = \sqrt{3J_2} = \sqrt{\frac{3}{2}} |\boldsymbol{\sigma}^D|, \tag{6}$$

3

is the von Mises stress; J_2 is the second deviatoric stress invariant,

$$J_2 = \frac{1}{2} \sum_{i,j=1}^{d} \left(\sigma_{ij}^D \right)^2 , \tag{7}$$

and $\boldsymbol{\sigma}^D = \boldsymbol{\sigma} - \frac{1}{3} tr(\boldsymbol{\sigma}) \mathbf{I}$ is the deviatoric part of stress tensor; $|\boldsymbol{\sigma}^D|$ denotes the Frobenius norm of deviatoric stress,

$$|\boldsymbol{\sigma}^D| = \left(\sum_{i,j=1}^{d} \left(\sigma_{ij}^D \right)^2 \right)^{1/2} . \tag{8}$$

If the von Mises stress, σ_v, tends to σ_y, the material stops behaving elastically and plastic yielding occurs. A popular flow rule for such material, e.g. Aluminium, is von Mises flow function considering linear isotropic hardening law,

$$\sigma_y = \sigma_0 + \gamma^{\mathrm{iso}} |\boldsymbol{\varepsilon}^p| , \tag{9}$$

where $\gamma^{\mathrm{iso}} > 0$ is the isotropic hardening parameter.

By applying a projector onto the set of admissible stresses, a primal problem can be formulated [28]. For the case of isotropic media with linear isotropic hardening, the 4$^{\mathrm{th}}$ order material property tensor is defined as [36]

$$\mathbb{C} = \mathbb{C}(\boldsymbol{\varepsilon}(\mathbf{u})) = \begin{cases} \mathbb{C}_\mu + \mathbb{C}_\kappa , & \sigma_v \leq \sigma_0 , \\ \mathbb{C}_\mu [\gamma + (1-\gamma)\frac{\sigma_0}{\sigma_v}] + \mathbb{C}_\kappa , & \sigma_v > \sigma_0 , \end{cases} \tag{10}$$

where

$$\mathbb{C}_\mu = 2\mu(\mathbb{I} - \mathbf{I} \otimes \mathbf{I}), \qquad \mathbb{C}_\kappa = \kappa \mathbf{I} \otimes \mathbf{I} . \tag{11}$$

$\mathbf{I}$ is the rank-2 unit symmetric tensor and $\mathbb{I}$ is the rank-4 identity tensor; μ and κ are the shear modulus and bulk modulus, respectively.

By applying Eq. (10), the stress tensor can be calculated as

$$\boldsymbol{\sigma} = \mathbb{C}(\boldsymbol{\varepsilon}(\mathbf{u})) : \boldsymbol{\varepsilon}(\mathbf{u}) . \tag{12}$$

For computing σ_v in Eq. (10), the elasticity formulation is assumed, $\mathbb{C}^e = \mathbb{C}_\mu + \mathbb{C}_\kappa$.

2.2. Variational form

For the elastoplasticity problem, the primal variational formulation has the following nonlinear form

$$a(\mathbf{u})(\mathbf{v}) = f(\mathbf{v}) , \qquad \mathbf{u} \in \mathbf{V}, \forall \mathbf{v} \in \mathbf{V}_0 , \tag{13}$$

with

$$a(\mathbf{u})(\mathbf{v}) = (\mathbb{C} : \boldsymbol{\varepsilon}(\mathbf{u}), \boldsymbol{\varepsilon}(\mathbf{v})) , \tag{14}$$

$$f(\mathbf{v}) = (\mathbf{f}, \mathbf{v}) + (\bar{\mathbf{t}}, \mathbf{v})_{\Gamma_n} , \tag{15}$$

4

in the space

$$\mathbf{V}_0 = \{\mathbf{v} \in \left[H^1(\Omega)\right]^d : \mathbf{v} = 0 \ \text{on} \ \Gamma_d\} \tag{16}$$

In order to solve the primal formulation (13), a damped Newton method is applied. Firstly, linearization should be performed and a method similar to the frequently used radial-return mapping algorithm [36, 37] is adopted. In case of replacing the complementarity condition by an equality using a Chen-Mangasarian smooth function [33], no return mapping algorithm is required [34, 35].

The solution is updated at each iteration, $\Delta \mathbf{U}_{n+1}^{k+1} = \Delta \mathbf{U}_n^{k+1} + \alpha_{n+1} \delta \mathbf{U}_{n+1}^{k+1}$. α_{n+1} is called step length and can be calculated when $\delta \mathbf{U}_{n+1}^{k+1}$ is known. As a result, we derive the equations for $\delta \mathbf{U}_{n+1}^{k+1}$ supposing that $\alpha_{n+1} = 1$. Consequently, $\delta \mathbf{U}_{n+1}^{k+1} = \Delta \tilde{\mathbf{U}}_{n+1}^{k+1} - \Delta \mathbf{U}_n^{k+1}$ can be calculated.

By applying the full Newton method, the following equation needs to be solved at each load/displacement increment k and Newton iteration n:

$$\left(\mathbb{C}^{lin}(\varepsilon_n^{k+1}) : \Delta\varepsilon(\Delta\tilde{\mathbf{u}}_{n+1}^{k+1}), \varepsilon(\mathbf{v})\right) = \left(f^{k+1}, \mathbf{v}\right) - \left(\boldsymbol{\sigma}_n^{k+1}, \varepsilon(\mathbf{v})\right) \tag{17}$$
$$+ \left(\mathbb{C}^{lin}(\varepsilon_n^{k+1}) : \Delta\varepsilon_n^{k+1}, \varepsilon(\mathbf{v})\right),$$

where $\mathbb{C}^{lin}(\varepsilon)$ denotes the linearization of the material property tensor (Eq. (10)) around $\varepsilon^D(\mathbf{u}_n^{k+1})$ [36],

$$\mathbb{C}^{lin} = \mathbb{C}^{lin}(\varepsilon(\mathbf{u})) = \begin{cases} \mathbb{C}_\mu + \mathbb{C}_\kappa, & \sigma_v \leq \sigma_0, \\ \\ \mathbb{C}_\mu[\gamma + (1-\gamma)\frac{\sigma_0}{\sigma_v}] + \mathbb{C}_\kappa \\ -2\mu(1-\gamma)\frac{\sigma_0}{\sigma_v}(\frac{\boldsymbol{\sigma}^D}{|\boldsymbol{\sigma}^D|} \otimes \frac{\boldsymbol{\sigma}^D}{|\boldsymbol{\sigma}^D|}), & \sigma_v > \sigma_0. \end{cases} \tag{18}$$

The initial solution field is considered zero,

$$\mathbf{U}^0 = 0, \quad \Delta\mathbf{U}_0^{k+1} = 0, \tag{19}$$

and the initial history stress and strain field, which are stored at the Gauss points, are defined as

$$\boldsymbol{\sigma}^0 = 0, \quad \varepsilon^0 = 0, \quad \boldsymbol{\sigma}_0^{k+1} = \boldsymbol{\sigma}^k.$$

By applying Eq. (17) and using the line search method [38], $\Delta\mathbf{U}_{n+1}^{k+1}$ is computed. Then, $\Delta\varepsilon_{n+1}^{k+1}$ can be calculated by taking its symmetric gradient,

$$\Delta\varepsilon_{n+1}^{k+1} = \nabla^{\text{sym}}(\Delta\mathbf{u}_{n+1}^{k+1}), \tag{20}$$

yielding subsequently

$$\varepsilon_{n+1}^{k+1} = \varepsilon^k + \Delta\varepsilon_{n+1}^{k+1}, \tag{21}$$

$$\boldsymbol{\sigma}_{n+1}^{k+1} = \mathbb{C}(\varepsilon_{n+1}^{k+1}) : \varepsilon_{n+1}^{k+1}. \tag{22}$$

Afterwards, the next iteration is started if the convergence criterion is not satisfied. Otherwise the solution field, $\mathbf{U}^{k+1}$, and history fields, $\boldsymbol{\sigma}^{k+1}$, ε^{k+1}, are updated and we can start the next increment procedure.

$$\mathbf{U}^{k+1} = \mathbf{U}^k + \Delta\mathbf{U}_{n+1}^{k+1}. \tag{23}$$

Fig. 1 demonstrates the general algorithm of the applied damped Newton procedure at the $(k+1)^{\text{th}}$ load/displacement increment.
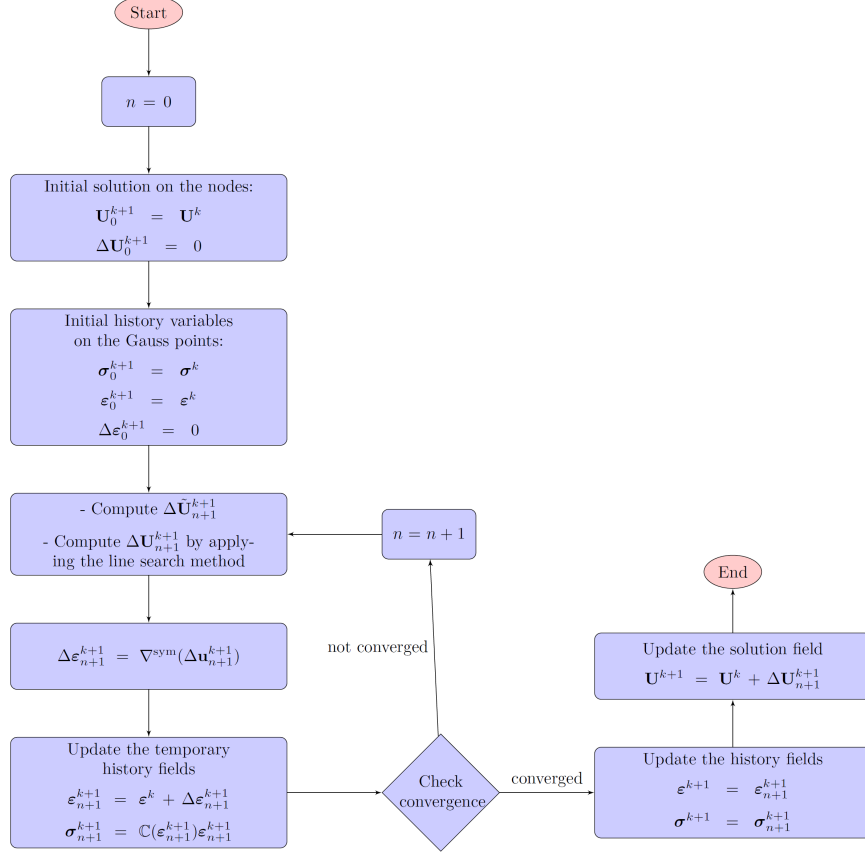

Figure 1: General algorithm of damped Newton process at the load/displacement increment $k+1$.

3. GOAL-ORIENTED ERROR ESTIMATION

The Goal-Oriented Error Estimation (GOEE) has been developed in order to estimate the error in a quantity of interest, e.g. displacement at a point or the average stress over a region. In GOEE besides the main (primal) problem, the solution of a dual/auxiliary problem is required.

The primal problem is the main problem defined in Eq. (13). By discretizing the domain into finite elements, the following variational formulation is obtained

$$a(\mathbf{u}^h)(\mathbf{v}^h) = f(\mathbf{v}^h) \qquad \forall \mathbf{v}^h \in \mathbf{V}_0^h \tag{24}$$

with subspaces $\mathbf{V}_0^h \subset \mathbf{V}_0$. In the following section, the dual problem is described.

3.1. Dual problem

The QoI can be described as a continuous linear functional, $J(\mathbf{u})$, on the space of admissible functions. If the QoI functional is non-linear, it may be linearized and then be used [21, 39]. Sometimes the functional may not be continuous, for instance, when we seek the solution error at a particular point in the domain. Therefore, the evaluation of a QoI functional, $J(\mathbf{u})$, is of interest rather than the solution values, $\mathbf{u}$, in the entire domain. The GOEE approximates the error in the QoI, $J(\mathbf{e}) = J(\mathbf{u}) - J(\mathbf{u}^h)$.

3.1.1. Elasticity problem

The dual problem for the elasticity problem is written in the form [25, 30]

$$a(\mathbf{v}, \mathbf{z}) = J(\mathbf{v}) \qquad \forall \mathbf{v} \in \mathbf{V}_0 \,, \tag{25}$$

where $a(\cdot, \cdot)$ is the bi-linear form associated with the elasticity problem and $\mathbf{z}$ denotes the solution. Then, by considering $\mathbf{v} = \mathbf{e} = \mathbf{u} - \mathbf{u}^h$ as the error, we have

$$J(\mathbf{e}) = a(\mathbf{e}, \mathbf{z}) \,, \tag{26}$$

which can be rewritten in the following form by applying the Galerkin orthogonality,

$$J(\mathbf{e}) = a(\mathbf{e}, \mathbf{z} - \mathbf{z}^h) = a\left(\mathbf{e}, \mathbf{e}^Q\right) \,, \tag{27}$$

where $\mathbf{z}^h \in \mathbf{V}^h$ is an approximation of $\mathbf{z}$ which is considered here as point interpolation of the dual solution, $\mathbf{z}^h = I^h \mathbf{z}$. Splitting the global integration over Ω into subdomains accounting for the contribution of the elements $K \in \mathbb{T}^h$ and integrating by parts element-wise yields

$$J(\mathbf{e}) = \sum_{K \in \mathbb{T}^h} \left\{ \left(-\nabla \cdot [\mathbb{C} : \varepsilon(\mathbf{e})], \mathbf{e}^Q \right)_K + \left(\mathbf{n} \cdot [\mathbb{C} : \varepsilon(\mathbf{e})], \mathbf{e}^Q \right)_{\partial K} \right\} \tag{28}$$

Knowing that $-\nabla \cdot [\mathbb{C} : \varepsilon(\mathbf{u})] = f$ and with the traction continuity of $\mathbf{n} \cdot [\mathbb{C} : \varepsilon(\mathbf{u})]$ across inter element edges, the error is represented as

$$J(\mathbf{e}) = \sum_{K \in \mathbb{T}^h} \left\{ \left(\mathbf{R}^h, \mathbf{e}^Q \right)_K + \left(\mathbf{r}^h, \mathbf{e}^Q \right)_{\partial K} \right\} \tag{29}$$

where K and ∂K denote an element and its boundary, respectively. The edge and element residuals are calculated as follows:

$$\mathbf{r}^h|_\Gamma = \begin{cases} \frac{1}{2}\mathbf{n} \cdot [\mathbb{C}(\boldsymbol{\varepsilon}(\mathbf{u}^h))\boldsymbol{\varepsilon}(\mathbf{u}^h)], & \text{if } \Gamma \subset \partial K \setminus \partial\Omega, \\ \bar{\mathbf{t}} - \mathbf{n} \cdot \mathbb{C}(\boldsymbol{\varepsilon}(\mathbf{u}^h))\boldsymbol{\varepsilon}(\mathbf{u}^h), & \text{if } \Gamma \subset \Gamma_n, \\ 0, & \text{if } \Gamma \subset \partial\Omega \setminus \Gamma_n. \end{cases} \qquad (30)$$

$$\mathbf{R}^h|_k = \mathbf{f} + \nabla \cdot \boldsymbol{\sigma} = \mathbf{f} + \nabla \cdot [\mathbb{C}(\boldsymbol{\varepsilon}(\mathbf{u}^h)) : \boldsymbol{\varepsilon}(\mathbf{u}^h)]. \qquad (31)$$

The edge residual, $\mathbf{r}^h|_\Gamma$, is obtained by exchanging half of the edge integral of the element K with its neighbor element K' and considering the opposite sign of their normal vectors.

3.1.2. Elastoplasticity problem

Considering that the semilinear form $a(\cdot)(\cdot)$ in Eq. (13) is not differentiable, the formal approach developed for the elasticity problem [25, 30] explained in Sec. 3.1.1 cannot be used directly. However, we can apply it heuristically for deriving weighted a posteriori error estimators in the FEM approximation [17]. Afterwards, it needs to be verified by numerical investigations. Its success can be explained by theoretical justification that the non-differentiability of the function $\mathbb{C}$ occurs solely in the elastic-plastic transition zone which is expected to be lower-dimensional [17]. Consider the following approximate dual problem

$$\left(\mathbb{C}^{lin}(\boldsymbol{\varepsilon}(\mathbf{u}^h)) : \boldsymbol{\varepsilon}(\mathbf{v}), \boldsymbol{\varepsilon}(\mathbf{z})\right) = J(\mathbf{v}), \qquad \forall \mathbf{v} \in \mathbf{V}_0. \qquad (32)$$

where $\mathbb{C}^{lin}(\cdot)$ is defined in Eq. (18). It is noted that the dual problem is formed based on the converged solution of the primal problem and is linear. The following error in the QoI can be obtained by applying the formal procedure of the DWR error estimation in the elasticity problem [17] and discretizing the domain into meshes $\mathbb{T}^h$.

$$J(\mathbf{e}) = \sum_{K \in \mathbb{T}^h} \left\{ \left(\mathbf{R}^h, \mathbf{z} - \mathbf{z}^h\right)_K + \left(\mathbf{r}^h, \mathbf{z} - \mathbf{z}^h\right)_{\partial K} \right\} + \mathbf{R}^{h(2)}, \qquad \mathbf{z}^h \in \mathbf{V}^h. \quad (33)$$

The remainder term $R^{h(2)}$ is quadratic in the error $\mathbf{e}$ in regions where the function $\mathbb{C}$ is twice differentiable. The elasto-plastic transition zone is the questionable region, since regularity fails. This term is neglected. The edge residual $\mathbf{r}^h$ and element residual $\mathbf{R}^h$ are given in Eqs. (30) and (31), respectively. The final form of (33) can be obtained by setting the discrete function $\mathbf{z}^h$, which is arbitrary, to the point interpolation of the dual solution, $\mathbf{z}^h = I^h\mathbf{z}$,

$$J(\mathbf{e}) = \sum_{K \in \mathbb{T}^h} \left\{ \left(\mathbf{R}^h, \mathbf{z} - I^h\mathbf{z}\right)_K + \left(\mathbf{r}^h, \mathbf{z} - I^h\mathbf{z}\right)_{\partial K} \right\}. \qquad (34)$$

Eq. (34) represents the error of the finite element discretization with respect to the functional $J(\cdot)$. The Dual Weighted Residual (DWR) is a weighted form of the residual error estimator, where $\mathbf{z} - I^h\mathbf{z}$ are weights indicating the importance of the element-wise residuals for the evaluation of the given functional. Since it

8

is an element-wise quantity, it can be applied as a mesh adaptation criterion. However, the DWR requires the dual solution $\mathbf{z}$, which conveys the information about the quantity of interest. For this purpose, we compute the dual solution numerically, and approximate $\mathbf{z}$ by some numerically obtained $\tilde{\mathbf{z}}$. It is noted that we cannot apply the same method as used for solving the primal solution $\mathbf{u}^h$, otherwise $\mathbf{z} - I^h \mathbf{z} = 0$, and the overall error estimate would be zero. Rather, the approximation $\tilde{\mathbf{z}}$ has to be from a larger space than the primal finite element space. There are various ways to obtain such an approximation. In this paper, we compute it in one higher order finite element space.

3.2. Quantity of interest functional

The dual problem, Eq. (32), is defined by a functional corresponding to the quantity of interest. In this contribution three quantities including the point displacement and average value of stress on a specific surface and in a region are of interest. If the QoI functional is non-linear, it can be linearized and then be used [21, 39]. Such a treatment is performed where average stress over a region is of interest.

3.2.1. Displacement at a point

Firstly, consider the displacement $\mathbf{u}(\mathbf{x}_0)$ at a point $\mathbf{x}_0$ as the quantity of interest. By using the definition of the Dirac delta function, δ, the corresponding functional is defined as

$$J(\mathbf{v}) = \mathbf{v}(\mathbf{x}_0) = \int_\Omega \mathbf{v}\delta(\mathbf{x} - \mathbf{x}_0)d\Omega\,. \tag{35}$$

3.2.2. Average stress on a surface

As a second quantity of interest, consider the mean value of a stress component $\sigma_{ij}^{av}|_S\,(i,j = x,y\,(,z))$ on a specified edge S in 2d or area S in 3d. The quantity of interest functional can be written as

$$J(\mathbf{v}) = \frac{1}{|\Gamma_S|}\int_{\Gamma_S}\sigma_{ij}(\mathbf{v})d\Gamma, \qquad i,j = x,y,z\,. \tag{36}$$

where $|\Gamma_S|$ is the length of the edge S in 2d or the area of the surface S in 3d. Although this QoI is a nonlinear functional for the elastoplastic problem, we do not linearize it since it is computed on the (element) boundary and its linearized form needs 2nd derivative of the solution and we would rather apply linearization where an (element) domain is considered and a dual problem of 2nd order or higher is defined.

3.2.3. Average stress in a region

The other quantity of interest which is investigated in this study is the mean value of a stress component $\sigma_{ij}^{av}|_{\Omega_0}\,(i,j = x,y,z)$ in a region Ω_0. Consequently, the following functional is introduced

$$J(\mathbf{v}) = \frac{1}{|\Omega_0|}\int_{\Omega_0}\sigma_{ij}(\mathbf{v})d\Omega, \qquad i,j = x,y,z\,, \tag{37}$$

9

where $|\Omega_0|$ is the volume of the region Ω_0 in the 3d case. Since the stress is a nonlinear function of displacement $\mathbf{u}$, Eq. (37) is a nonlinear functional.

In such a case, we need to firstly linearize the functional to apply the goal-oriented error estimation methodology. For this purpose, we utilize the Taylor expansion,

$$
\begin{aligned}
J(\mathbf{u}) &= J(\mathbf{u}^h) + \nabla J(\mathbf{u}^h) \cdot (\mathbf{u} - \mathbf{u}^h) + \cdots \\
&= J(\mathbf{u}^h) + \nabla J(\mathbf{u}^h) \cdot \mathbf{e} + \cdots ,
\end{aligned}
\tag{38}
$$

$$
J(\mathbf{u}) - J(\mathbf{u}^h) \cong \nabla J(\mathbf{u}^h) \cdot \mathbf{e} ,
\tag{39}
$$

$$
J^{lin}(\mathbf{e}) = \nabla J(\mathbf{u}^h) \cdot \mathbf{e} .
\tag{40}
$$

Subsequently, we can apply the aforementioned goal-oriented error estimation by replacing the QoI functional $J(\mathbf{v})$ in the dual problem, Eq. (25) for elasticity problem and Eq. (32) for elastoplasticity problem, with the linearized QoI functional

$$
J^{lin}(\mathbf{v}) = \nabla J(\mathbf{u}^h) \cdot \mathbf{v} .
\tag{41}
$$

where it is defined according to the approximated solution of the primal problem $\mathbf{u}^h$. Correspondingly, the QoI functional (37) is linearized as follows

$$
J^{lin}(\mathbf{v}) = \frac{1}{|\Omega_0|} \int_{\Omega_0} \nabla \sigma_{ij}(\mathbf{u}^h) \cdot \mathbf{v} d\Omega, \qquad i, j = x, y, z .
\tag{42}
$$

4. MESH ADAPTIVITY

Error estimation is carried out at the end of each load/displacement increment. If the estimated error is higher than the prescribed error limit, mesh adaptation is performed and the solution variables are projected onto the new mesh. Except for the first load/displacement increment, mesh adaptation is allowed only once. The whole schematic procedure is depicted in Fig. 2.
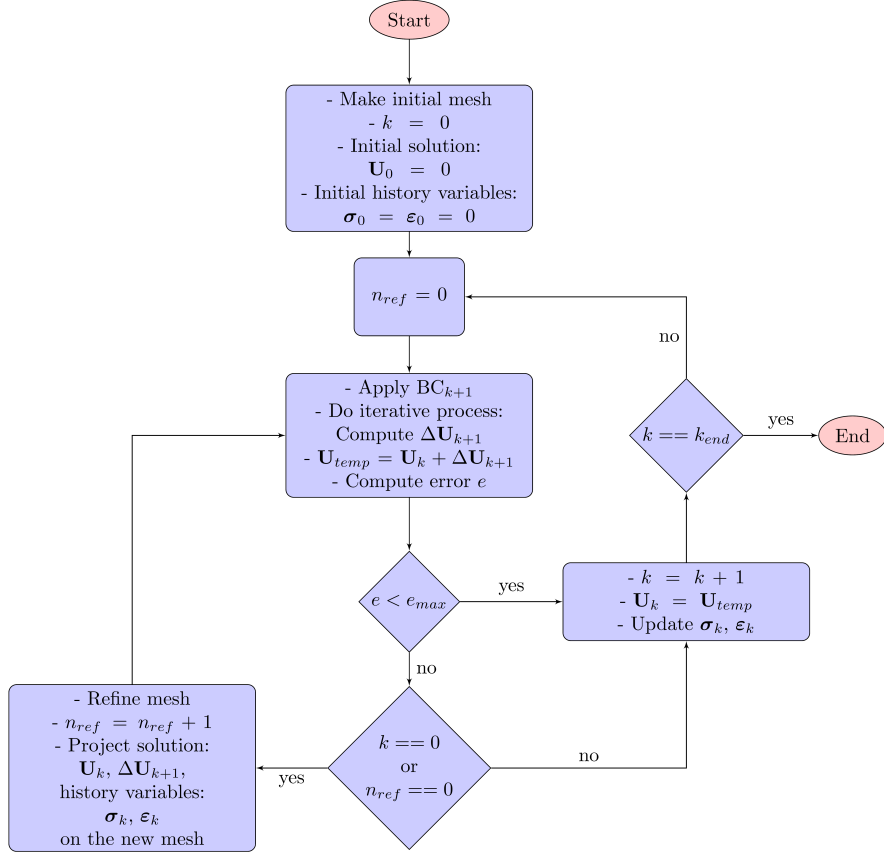
Figure 2: General algorithm for error estimation and mesh adaptivity in elastoplasticity problem.

Since solution variables need to be transferred from the previous mesh to the new mesh after each mesh adaptation, hierarchical mesh refinement and coarsening is performed in order to increase the efficiency. Quadrilateral and hexahedral elements are applied in this work and are splitted into 4 and 8 elements, respectively, in the refinement process by dividing each edge into 2 equal segments. Therefore, refinement introduces hanging nodes. The hanging nodes are constrained to be compatible with adjacent nodes, so that the function has no jump at the boundary of small and large elements. It is performed by defining the solutions of hanging nodes as linear combinations of their neighboring nodes' solutions and correspondingly constructing a constraint matrix.

Mesh adaptation is carried out with the knowledge of element-wise errors. Calculated errors are firstly sorted. The 30 percent of the elements with the highest errors are selected to be refined and the 3 percent of those with lowest errors are chosen to be coarsened though other percentages can be specified by

the user.

The difference of neighboring elements' refinement level should not exceed one. Therefore, some adjacent elements of the selected elements for refinement need to be refined too. For the same reason, some marked elements for coarsening are not allowed to be coarsened (changed to its one lower refinement level).

After each adaptivity level, the degrees of freedom in the new mesh are enumerated.

There exist other adaptivity algorithms which have been specifically developed for fracture modeling (see [40–42]).

5. NUMERICAL EXAMPLES

Three numerical examples are presented subsequently. In addition to the goal-oriented mesh adaptivity process, global refinement and mesh adaptivity based on the recovery-based error estimation developed by Kelly et al. [43] and residual-based error estimation (based on edge and cell residuals given in Eqs. (30) and (31)) are also performed. In the global refinement process, all elements are uniformly subdivided by 4 and 8 elements at each refinement step in the 2d and 3d cases, respectively.

5.1. Thick tube subjected to internal pressure

In order to verify the proposed approach, an example with available analytical solution is considered. Consider an elastic perfectly plastic thick tube in the plane strain state subjected to uniform internal pressure. As a result of the geometry and loading symmetries, one quarter is only modeled (see Fig. 3).
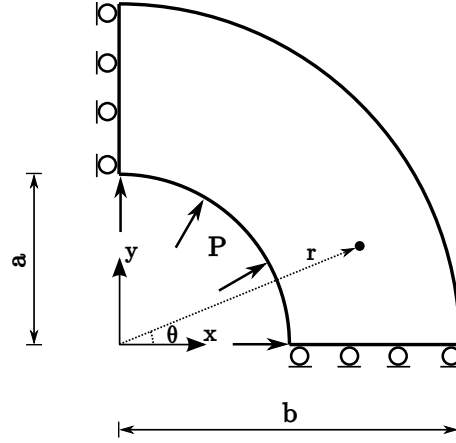

Figure 3: Geometry and boundary conditions of the thick tube subjected to uniform internal pressure.

The following geometry and material parameters are considered: Inner radius $a = 100$ mm, outer radius $b = 200$ mm, yield strength $\sigma_y = 240$ MPa, Young's modulus $E = 210$ GPa and Poisson's ratio $\nu = 0.3$.

12

If the imposed internal pressure, P_i, is sufficiently small, the entire tube remains elastic. However, when P_i becomes large enough, the tube begins to yield from the inner surface $r = a$. With the continuous increase of P_i the yielded region will expand outwards. From symmetry it follows that the elasto-plastic interface is also a cylindrical surface for any value of P_i that produces a plastic region. Let r_c be the radius of this elasto-plastic interface, and P_c be the associated pressure acting on the interface under P_i (a generic value). Then, the material in the region $a \leq r \leq r_c$ is in the plastic state, whereas the material in the region $r_c \leq r \leq b$ remains elastic under P_i.

The radius of elasto-plastic interface, r_c, can be calculated by solving the following equation [44],

$$P_i = \frac{\sigma_y}{\sqrt{3}} \left[1 - \frac{r_c^2}{b^2} + 2 \ln \frac{r_c}{a} \right], \tag{43}$$

where σ_y is the yield strength of the material.

The analytical stress and displacement solutions in the polar coordinates for the plastic and elastic regions, are as follows:

- Plastic region ($a \leq r \leq r_c$):

$$\sigma_{rr} = \frac{\sigma_y}{\sqrt{3}} \left[-1 + \frac{r_c^2}{b^2} - 2 \ln \frac{r_c}{r} \right], \qquad \sigma_{\theta\theta} = \frac{\sigma_y}{\sqrt{3}} \left[1 + \frac{r_c^2}{b^2} - 2 \ln \frac{r_c}{r} \right] \tag{44}$$

$$u_r = \frac{\sqrt{3}}{2} \frac{\sigma_y}{E} \frac{r_c^2}{r} . \tag{45}$$

- Elastic region ($r_c \leq r \leq b$):

$$\sigma_{rr} = \frac{P_c r_c^2}{b^2 - r_c^2} \left(1 - \frac{b^2}{r^2} \right), \qquad \sigma_{\theta\theta} = \frac{P_c r_c^2}{b^2 - r_c^2} \left(1 + \frac{b^2}{r^2} \right), \tag{46}$$

$$u_r = \frac{1+\nu}{E} \frac{P_c r_c^2}{b^2 - r_c^2} \left(1 - 2\nu + \frac{b^2}{r^2} \right) r \tag{47}$$

where P_c is the pressure on the elasto-plastic interface, $r = r_c$, which can be calculated from Eq. (44),

$$P_c = -\sigma_{rr}|_{r=r_c} = -\frac{\sigma_y}{\sqrt{3}} \left[-1 + \frac{r_c^2}{b^2} \right] . \tag{48}$$

The initial discretization (192 elements) is shown in Fig. 4. Several simulations with constant load increments, $\Delta P = 1, 6, 24, 192$ MPa, are performed.
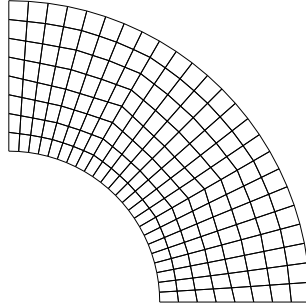

Figure 4: Initial discretization for modeling the thick tube.

13

Fig. 5 demonstrates the variation of load factor P_i/σ_y with the non-dimensionalized displacement $4\mu u_a/(\sigma_y a)$ at the inner radius for different load increment steps besides the theoretical solution [44], obtained by using Eqs. (43), (47) and (45). μ is shear modulus and u_a is the radial displacement at the inner radius $r = a$. A slight discontinuity is observed in the analytical solution when the inner radius enters the plasticity, $r_c = 0.1$ and $P_i/\sigma_y = 0.433013$, since the plastic deformation formulations were derived with the assumption of incompressibility. It is seen that the numerical results are in good agreement with analytical solutions. Elements of the first layer of the model, with incremental load $\Delta P = 1$ MPa, enters into plasticity when $P_i = 113$ MPa. Then, as the load increases, the elastic elements enters into plastic zone gradually and the whole model becomes plastic when $P_i = 194$ MPa.
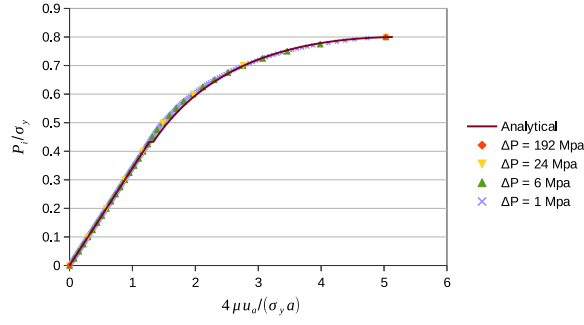

Figure 5: Non-dimensional load-displacement curve in the thick tube model.

Table 1 presents the non-dimensionalized load and displacement values as well as their corresponding exact error (%) for the case $\Delta P = 24$ MPa.

Table 1: Non-dimensionalized load and displacement values and their errors (%) for the case $\Delta P = 24$ MPa

Load step	$\frac{P_i}{\sigma_y}$	$\frac{4\mu u_a}{\sigma_y a}\big|_{\text{simulation}}$	$\frac{4\mu u_a}{\sigma_y a}\big|_{\text{analytical}}$	Exact error (%)
1	0.1	0.2926	0.293333	0.25
2	0.2	0.5852	0.586667	0.25
3	0.3	0.8778	0.88	0.25
4	0.4	1.1703	1.173333	0.26
5	0.5	1.4822	1.562204	5.12
6	0.6	1.9657	2.026866	3.02
7	0.7	2.7618	2.771664	0.36
8	0.8	5.0289	5.138994	2.14

Fig. 6 illustrates the distribution of radial and hoop stresses along the radius for $P/\sigma_y = 0.6$. The presented stresses are the nodal stresses computed from nodal averaging technique. For their computation, firstly the stresses on the

14

Gauss points are transformed to the polar coordinates, then they are extrapolated to the nodes. Since at each node different values may be obtained from the adjacent elements, the average value is computed. The results agree well with the analytical solutions. The errors at the inner radius, $r = a$, are maximum and it is expected that more refinement near the inner radius, leads to higher accuracy.
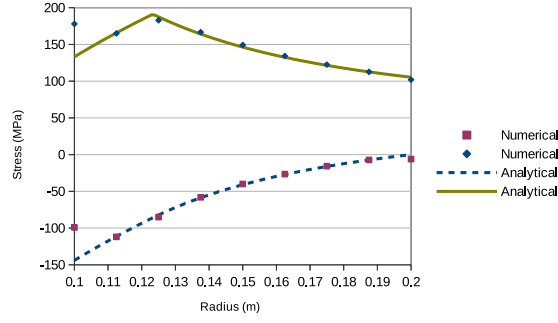

Figure 6: Distribution of σ_{rr} and $\sigma_{\theta\theta}$ (MPa) along radial direction for $P/\sigma_y = 0.6$.

Now, suppose that we intend to increase the accuracy in the numerically calculated stresses on the inner curve S when $P/\sigma_y = 0.6$. The corresponding functional, which is substituted in the right-hand side of Eq. (32), can be defined as

$$J(\mathbf{v}) = \frac{1}{|\Gamma_S|} \int_{\Gamma_S} \sum_{i,j} \sigma_{ij}(\mathbf{v}) d\Gamma, \qquad i, j = x, y, \tag{49}$$

where $|\Gamma_S|$ is the arc length S with radius, $r = 0.1$.

Incremental load $\Delta P = 24$ MPs is imposed. As a starting point of the adaptivity process, 48 elements (130 DoFs) are applied for the discretization (see Fig. 7 (a)). Different strategies including global refinement and adaptivity based on estimated errors by using Kelly, residual and goal-oriented error estimation, GOEE, have been tested. Each methodology leads to different element errors and therefore, the resulting meshes are different. Figs. 7 (b-d) illustrate the sample resulting meshes of different schemes. Fig. 7 (c) shows a non-uniform distribution of elements, probably due to the kinks along the element boundaries at the angles $\theta = 30\,^\circ$ and $\theta = 60\,^\circ$. The GOEE-based adaptivity leads to mesh concentration around the surface S where the quantity of interest has been defined.
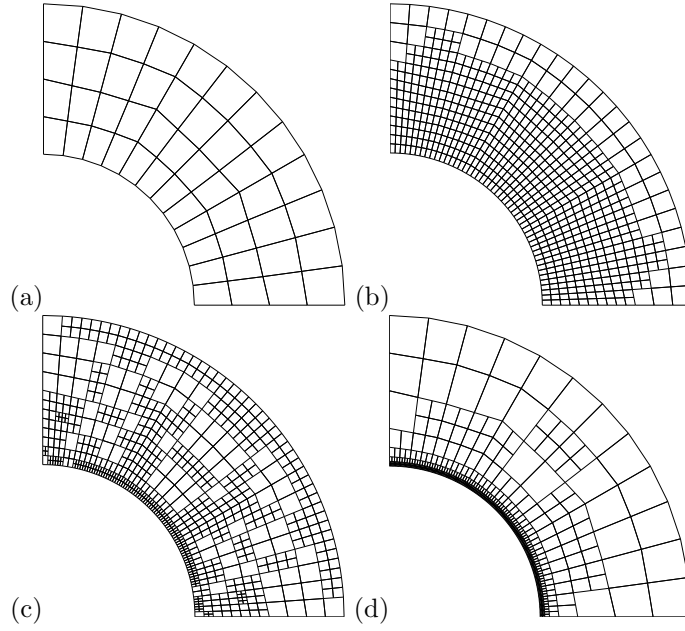
15

Figure 7: Discretizations of the thick tube model: (a) Initial mesh; meshes resulted in adaptivity process applying (b) Kelly error estimation with 630 elements, (c) Residual error estimation with 684 elements and (c) GOEE with 618 elements.

The relative errors in the $\sigma_{rr}^{av}|_S$ are depicted in Fig. 8. The goal-oriented error estimation results in an adaptivity process with better convergence rate. Very similar results are obtained for the $\sigma_{\theta\theta}^{av}|_S$.
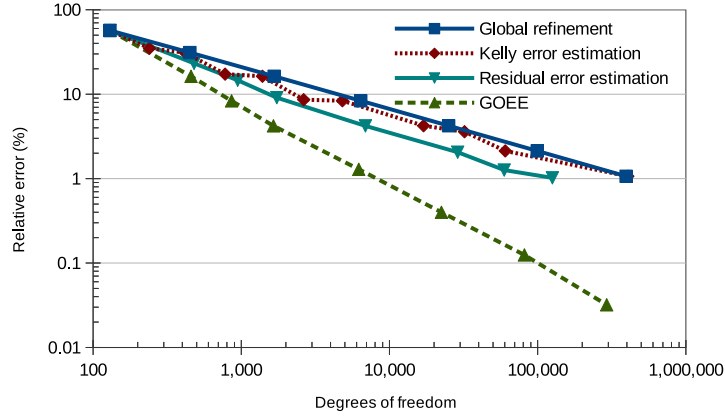

Figure 8: Exact relative errors (%) of $\sigma_{rr}^{av}|_S$ versus degrees of freedom for the thick wall subjected to internal pressure.

Fig. 9 illustrates the exact relative error (%) of $\sigma_{rr}^{av}|_S$ versus the consumed computational time (sec). It is shown that for achieving a precise solution of the quantity of interest, the proposed goal-oriented adaptivity is the most efficient method.
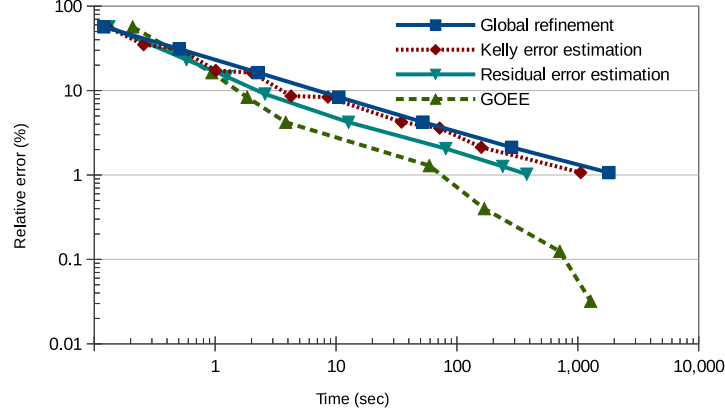

Figure 9: Exact relative errors (%) of $\sigma_{rr}^{av}|_S$ versus computational times (sec) for the thick wall subjected to internal pressure.

5.2. Round perforated strip under enforced displacement

Consider the perforated strip of strain-hardening material, which was studied experimentally by Theocaris and Marketos [45]. Due to the symmetry only a quarter of the strip is modeled (see Fig. 10), with length $L = 180$ mm, width $W = 100$ mm, perforation radius $R = 50$ mm and thickness $T = 4$ mm. The material used was an aluminium alloy 57S with a yield stress in pure tension $\sigma_y = 243$ MPa. Other material parameters are: Elastic modulus $E = 70$ GPa, Poisson's ratio $\nu = 0.3$ and plastic modulus $\gamma^{iso} = 2\mu\frac{\gamma}{1-\gamma} = 2.25$ GPa which leads to $\gamma = 0.0401097$.
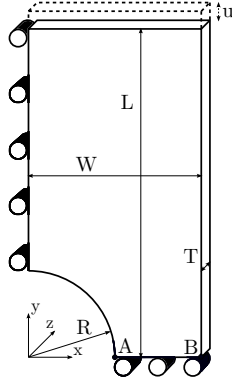

Figure 10: Geometry and loading of a perforated strip subjected to imposed displacement.

17

The mean stress component σ_{yy} on the bottom surface S, where $y = 0$, is considered as the quantity of interest:

$$J(\mathbf{v}) = \frac{1}{|\Gamma_S|} \int_{\Gamma_S} \sigma_{yy}(\mathbf{v})d\Gamma\,, \qquad (50)$$

where $|\Gamma_S|$ is the area of surface S.

A displacement $u = 0.55$ mm as shown in Fig. 10 is imposed at the top surface incrementally in 22 steps. The initial mesh consisting of 192 elements and the goal-oriented refined mesh composed of 1830 elements are shown in Fig. 11.
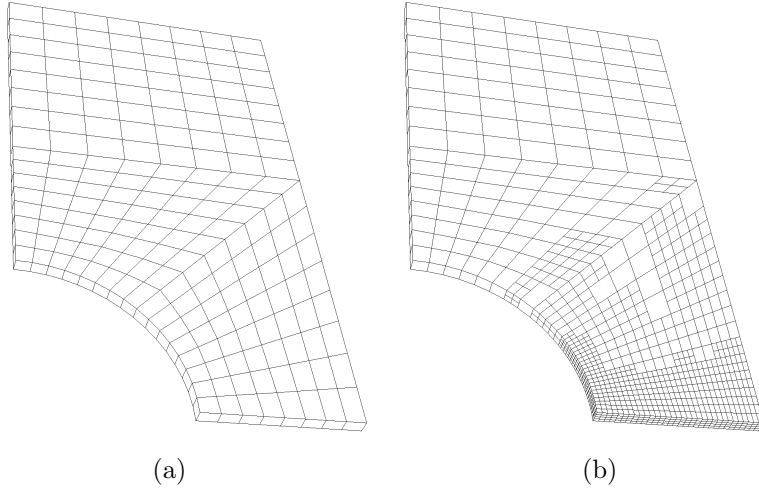

(a)　　　　　　　　　　　　　　　(b)

Figure 11: Discretization of the perforated strip subjected to imposed displacement: (a) Initial mesh (192 elements); (b) Refined mesh applying Goal-oriented adaptivity (1830 elements).

Fig. 12 illustrates the relation between the non-dimensional average stress on the bottom surface, $\sigma_{yy}^{av}/\sigma_y$, and the non-dimensional strain at point A, $E\varepsilon_{yy}^A/\sigma_y$. Fig. 12 also includes the experimental results which were extracted by reading the values from the plots provided in [45].
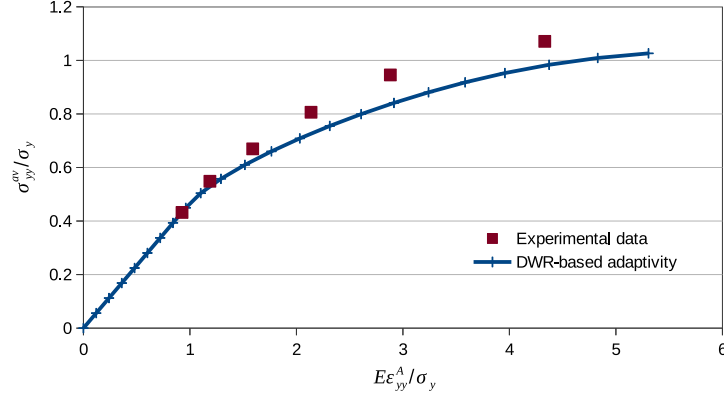
Figure 12: Non-dimensional relation between σ_{yy}^{av} and ε_{yy} at Point A.

The computed strain is larger than the experimentally observed strain. Other invistigators reported similar discrepancies. A possible explanation is that in the case of the numerical simulation the strain is reported with an infinitesimal gauge length whereas experimentally determined strains invariably involve some gauge length of finite size.

Fig. 13 depicts the distribution of normalized stress σ_{yy}/σ_y along AB ($y = z = 0$) at step 19 where the imposed displacment is $u = 0.475$ mm. The results are in good agreement with experimental data [45]. The σ_{yy} stress distribution at the same step is also illustrated in Fig. 14 for the whole domain.
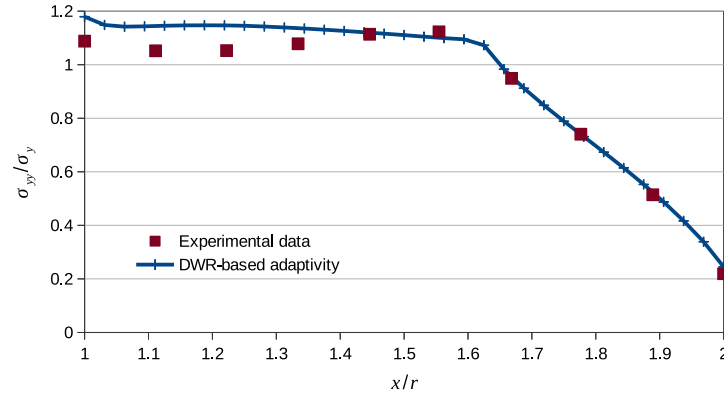

Figure 13: Distribution of non-dimensional tensile stress σ_{yy} along AB at step 19 where the imposed displacement is $u = 0.475$ mm.
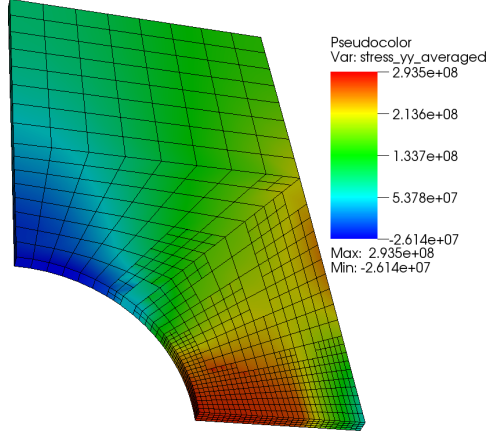
Figure 14: Distribution of stress component σ_{yy} at step 19 where the imposed displacement is $u = 0.475$ mm.

5.3. Cantiliver beam under surface pressure

Consider a rectangular tube made of aluminium alloy 57S, which is clamped at one end and subjected to surface pressure. The material is the same as in the previous example. The geometry and loading is shown in Fig. 15 with Length, $L = 70$ cm, width, $W = 8$ cm, height, $H = 20$ cm, web and flange thicknesses, $t_w = t_f = 1$ cm and surface pressure, $P = 6$ MPa.
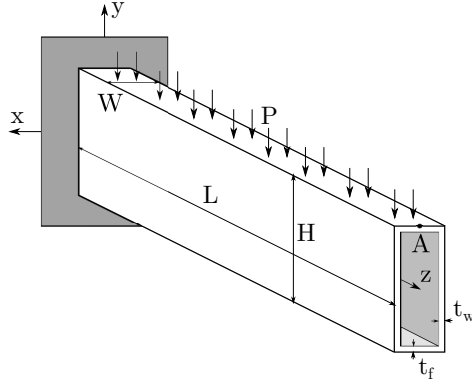
Figure 15: Geometry and loading of a cantilever beam subjected to pressure on the top surface.

In this example two different quantities of interest, QoI, are considered separately for the goal-oriented mesh adaptivity.

The first QoI is the displacement at Point A, $\mathbf{u}_A$, located in $x = 0, y = H/2, z = L$ (see Fig. 15). Accurate prediction of this QoI leads to a more precise load deflection curve which is important in materials design. By using

the definition of the Dirac delta function, δ, the corresponding functional is defined as

$$J(\mathbf{v}) = \mathbf{v}(\mathbf{x}_A) = \int_\Omega \mathbf{v}\delta(\mathbf{x} - \mathbf{x}_A)d\Omega \,. \tag{51}$$

Now, consider that we want to calculate the maximum von-Mises stress in the beam which is important to predict the failure load accurately. Knowing that the maximum von Mises stress occurs at the flanges close to the clamped area, we define the QoI functional as the average value of all stress components in the domain, Ω_0, which consists of the first row of elements (in initial mesh) in the top and bottom flanges closed to the fixed area, $-W/2 \leq x \leq W/2$, $H/2 - t_f \leq y \leq H/2$, $-H/2 \leq y \leq -H/2 + t_f$, $0 \leq z \leq 2t_f$,

$$J(\mathbf{v}) = \frac{1}{|\Omega_0|} \int_{\Omega_0} \sum_{i,j} \sigma_{ij}(\mathbf{v})d\Omega, \qquad i,j = x, y, z \,, \tag{52}$$

and its corresponding linearized form is defined as

$$J^{lin}(\mathbf{v}) \quad = \quad \frac{1}{|\Omega_0|} \int_{\Omega_0} \sum_{i,j} \nabla\sigma_{ij}(\mathbf{u}^h) \cdot \mathbf{v}d\Omega, \qquad i,j = x, y, z \,. \tag{53}$$

The surface pressure P is applied in 10 loading steps. The mesh discretization consisting of 1820 elements shown in Fig. 16(a) is considered as the initial mesh. Global refinement and local refinement based on elementwise errors computed by applying Kelly, residual-based and goal-oriented error estimations are performed in 1-2 levels.

Fig. 16 shows the initial mesh and two-level adapted meshes resulted of applying different error estimations. In all cases except for the GOEE-based refinement, the refinement is performed in the first step and the computed errors in the rest steps remained below the specified value. In the GOEE-based refinement case based on the first QoI, $|u_y^A|$, the specified maximum relative error, 4.4e-5, leads to a refinemnt level in the first step and the second refinment level in the seventh step (see Fig. 16(d)). It is noted that the unsymmetrical meshes in Fig. 16(d) with respect to y-axis is the result of the unsymmetric dual problem, which determines the elementwise weights which affect the quality assessment of the $|u_y^A|$.
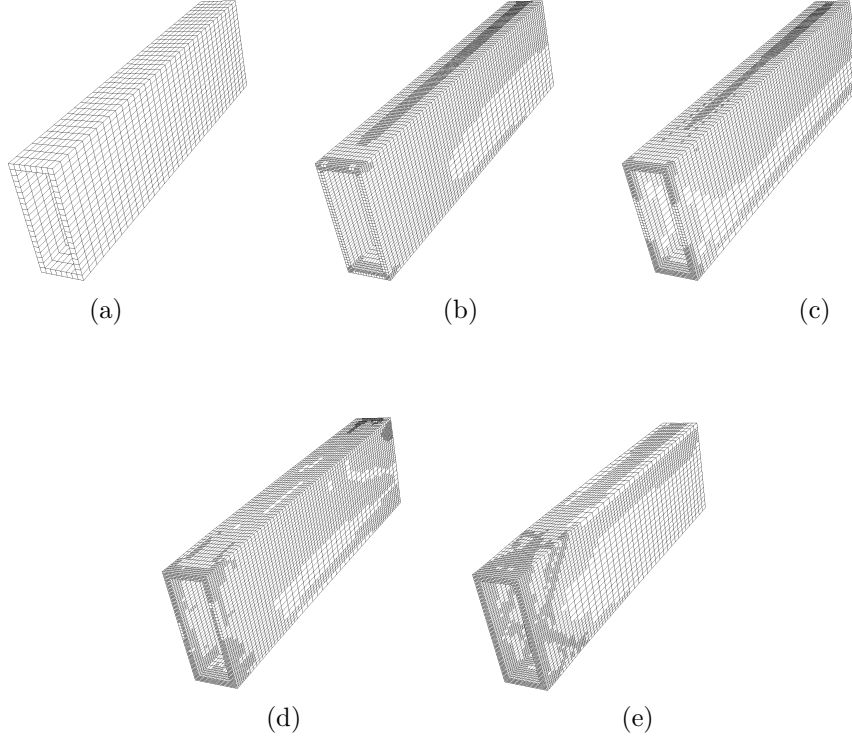
Figure 16: Discretization of the cantilever beam of rectangular tube: (a) Initial mesh (1 820 elements); Two-level refined meshes applying (b) Kelly error estimation(17 486 elements), (c) residual-based error estimation (17 500 elements), (d) GOEE (17 472 elements in step 8) considering the first QoI and (e) GOEE (17 486 elements in step 8) considering the second QoI.

Fig. 17 illustrates the load-deflection curve for initial mesh and global refinement cases. The number of degrees of freedom are 11 232, 66 456 and 439 920, respectively, for uniform refinements. It is observed that the results converges with increasing refinement.
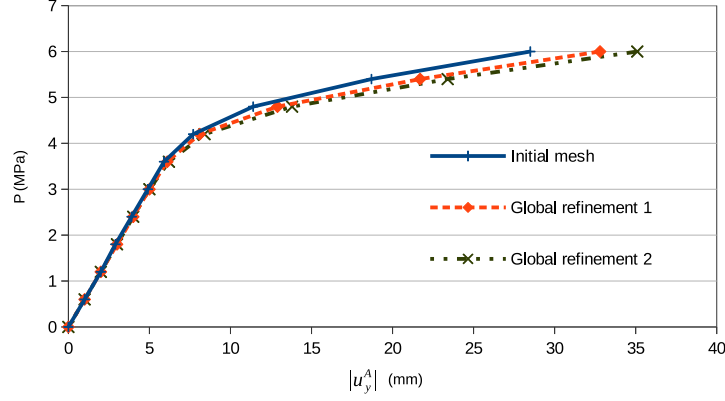
Figure 17: Relation between pressure, P, and absolute value of displacement at point A in y direction, $|u_y^A|$ for different global refinement.

The results of $|u_y^A|$ for all load steps and refinement strategies are given in Table 2. If we consider the computed $|u_y^A|$ in the global refinement 2, as the most accurate result which can be achieved in two refinement levels, it is observed that the Goal-oriented mesh adaptivity procedure results in more accurate result in comparison with other applied refinement methodologies.

Table 2: Resulted $|u_y^A|$ (mm) for different loading steps by applying several refinement strategies

	IM	GR 1	GR 2	KR 1	KR 2	RR 1	RR 2	GOEE
Elements	1820	14560	116480	5642	17486	5642	17500	5642, 17472
LS								
1	1	*1	**1	*1	**1	*1	**1	*1
2	2	2	2	2	2	2	2	2
3	2.9	3	3	3	3	3	3	3
4	3.9	4	4	4	4	4	4	4
5	4.9	5	5	4.9	5	4.9	5	4.9
6	5.9	6.1	6.2	6.1	6.1	6.1	6.1	6.1
7	7.7	8.1	8.4	8.1	8.2	8	8.3	**8.3
8	11.4	12.9	13.8	12.7	13.2	12.5	13.4	13.6
9	18.7	21.7	23.4	21.4	22.4	21.1	22.8	23
10	28.5	32.8	35.1	32.4	33.7	32.1	34.3	34.6

LS: Load step, IM: Initial mesh, GR: Global refinement,
KR: Kelly-based refinement, RR: Residual-based refinement,
*: First refinement step, **: Second refinement step

The GOEE-based mesh adaptivity is also performed considering the second

23

QoI and a prescribed maximum permissible error. Accordingly, refinement has been performed in the 6th and 8th steps. The mesh discretization in the 8th is depicted in Fig. 16(e). Fig. 18 demonstrates the von-Mises stress distribution and the plastic zones at the 8th loading step where the imposed pressure is $P = 4.8$ MPa.
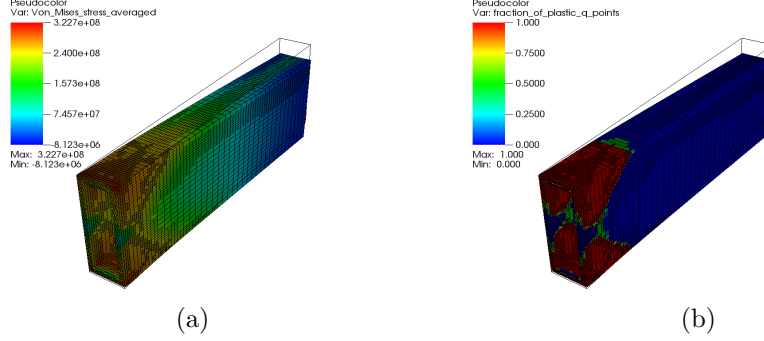

<div align="center">(a)   (b)</div>

Figure 18: (a) Von-Mises stress distribution and (b) Plastic zones: at 8th step computed by applying the goal-oriented mesh adaptivity. Displacemnts have been magnified by 3.

If we consider the maximum von-Mises stress computed in the two-level global refinement as the reference solution, we can compare the accuracy of GOEE results with those obtained by applying Kelly and residual-based error estimations. The corresponding relative errors of each model at loading steps 8-10 are given in Table 3. Comparison of results highlights the superiority of the proposed approach compared to the other conventional mesh refinement procedures.

Table 3: Relative error of maximum von-Mises stress (%) at loading steps 8-10 considering the solution in two-level global refined case as the reference solution.

	KR 2	RR 2	GOEE
Elements	17 486	17 500	17 486
Load step			
8	3.42	1.36	0.19
9	4.82	1.66	0.20
10	5.61	1.61	0.14

<div align="center">KR: Kelly-based refinement, RR: Residual-based refinement</div>

6. CONCLUSIONS

In this paper, a goal-oriented error estimation approach called Dual-Weighted Residual has been extended for adaptive mesh refinement in three-dimensional

elastoplasticity problems to quantify and control the local error in quantities of interest. At each load/displacement increment the error is computed and when it is greater than the prescribed maximum error, mesh adaptivity is performed and the solution from the old mesh is projected to the new mesh.

Several numerical examples with different quantities of interest have been investigated. By comparing the results with mesh adaptivity based on conventional recovery-based and residual-based error estimations, the superiority of the proposed approach has been illustrated. The results show that when a specific quantity is of interest, the goal-oriented adaptivity is a competitive computational approach to calculate it with high accuracy.

ACKNOWLEDGMENTS

REFERENCES

[1] V.P. Nguyen, T. Rabczuk, S.P.A. Bordas, and M. Duflot. Meshless methods: A review and computer implementation aspects. *Mathematics and Computers in Simulation*, 79(3):763 – 813, 2008.

[2] T. Rabczuk and T. Belytschko. Cracking particles: a simplified meshfree method for arbitrary evolving cracks. *International Journal for Numerical Methods in Engineering*, 61(13):2316–2343, 2004.

[3] S.Sh. Ghorashi, S. Mohammadi, and S.-R. Sabbagh-Yazdi. Orthotropic enriched element free galerkin method for fracture analysis of composites. *Engineering Fracture Mechanics*, 78(9):1906 – 1927, 2011.

[4] H. Khazal, H. Bayesteh, S. Mohammadi, S.Sh. Ghorashi, and A. Ahmed. An extended element free galerkin method for fracture analysis of anisotropic functionally graded materials. *Mechanics of Advanced Materials and Structures*, 2015.

[5] X. Zhuang, C.E. Augarde, and K.M. Mathisen. Fracture modeling using meshless methods and level sets in 3d: Framework and modeling. *International Journal for Numerical Methods in Engineering*, 92(11):969–998, 2012.

[6] T. Belytschko and T. Black. Elastic crack growth in finite elements with minimal remeshing. *International Journal for Numerical Methods in Engineering*, 45:601–620, 1999.

[7] S.Sh. Ghorashi, N. Valizadeh, and S. Mohammadi. Extended isogeometric analysis for simulation of stationary and propagating cracks. *International Journal for Numerical Methods in Engineering*, 89(9):1069–1101, 2012.

[8] Y. Jia, C. Anitescu, S.Sh. Ghorashi, and T. Rabczuk. Extended isogeometric analysis for material interface problems. *IMA Journal of Applied Mathematics*, 2014.

[9] S.Sh. Ghorashi, N. Valizadeh, S. Mohammadi, and T. Rabczuk. T-spline based {XIGA} for fracture analysis of orthotropic media. *Computers & Structures*, 147(0):138 – 146, 2015. CIVIL-COMP.

[10] N. Nguyen-Thanh, N. Valizadeh, M.N. Nguyen, H. Nguyen-Xuan, X. Zhuang, P. Areias, G. Zi, Y. Bazilevs, L. De Lorenzis, and Rabczuk. T. An extended isogeometric thin shell analysis based on kirchhoff-love theory. *Computer Methods in Applied Mechanics and Engineering*, 284: 265–291, 2015.

[11] I. Babuška and W. C. Rheinboldt. A-posteriori error estimates for the finite element method. *International Journal for Numerical Methods in Engineering*, 12(10):1597–1615, 1978.

[12] O. C. Zienkiewicz and J. Z. Zhu. A simple error estimator and adaptive procedure for practical engineering analysis. *International Journal for Numerical Methods in Engineering*, 24(2):337–357, 1987.

[13] O. C. Zienkiewicz and J. Z. Zhu. The superconvergent patch recovery and a posteriori error estimates. part 1: The recovery technique. *International Journal for Numerical Methods in Engineering*, 33(7):1331–1364, 1992.

[14] O. C. Zienkiewicz and J. Z. Zhu. The superconvergent patch recovery and a posteriori error estimates. part 2: Error estimates and adaptivity. *International Journal for Numerical Methods in Engineering*, 33(7):1365–1382, 1992.

[15] R. Becker and R. Rannacher. A feed-back approach to error control in finite element methods: Basic analysis and examples. *East-West J. Numer. Math*, 4:237–264, 1996.

[16] R. Becker and R. Rannacher. Weighted a posteriori error control in fe methods. In Bock, H. G. et al., ed.s, ENUMATH 95, pages 621637, Paris, September 1998. World Scientific Publ., Singapore., 1998.

[17] W. Bangerth and R. Rannacher. *Adaptive finite element methods for differential equations*. Birkhäuser Verlag, Basel, 2003.

[18] S. Prudhomme and J.T. Oden. On goal-oriented error estimation for elliptic problems: application to the control of pointwise errors. *Computer Methods in Applied Mechanics and Engineering*, 176(14):313 – 331, 1999.

[19] E. Stein, M. Rüter, and S. Ohnimus. Error-controlled adaptive goal-oriented modeling and finite element approximations in elasticity. *Computer Methods in Applied Mechanics and Engineering*, 196(3740):3598 – 3613, 2007. Special Issue Honoring the 80th Birthday of Professor Ivo Babuska.

[20] T. Pannachet, P. Díez, H. Askes, and L.J. Sluys. Error assessment and mesh adaptivity for regularized continuous failure models. *Computer Methods in Applied Mechanics and Engineering*, 199(1720):961 – 978, 2010.

[21] C. Zaccardi, L. Chamoin, R. Cottereau, and H. Ben Dhia. Error estimation and model adaptation for a stochastic-deterministic coupling method based on the arlequin framework. *International Journal for Numerical Methods in Engineering*, 96(2):87–109, 2013.

[22] O.A. González-Estrada, E. Nadal, J.J. Ródenas, P. Kerfriden, S.P.A. Bordas, and F.J. Fuenmayor. Mesh adaptivity driven by goal-oriented locally equilibrated superconvergent patch recovery. *Computational Mechanics*, 53 (5):957–976, 2014.

[23] J.P. Whiteley and S.J. Tavener. Error estimation and adaptivity for incompressible hyperelasticity. *International Journal for Numerical Methods in Engineering*, 99(5):313–332, 2014.

[24] E. Rabizadeh, A. Saboor Bagherzadeh, and T. Rabczuk. Adaptive thermo-mechanical finite element formulation based on goal-oriented error estimation. *Computational Materials Science*, 102:27 – 44, 2015.

[25] R. Rannacher and F.-T. Suttmeier. A feed-back approach to error control in finite element methods: application to linear elasticity. *Computational Mechanics*, 19(5):434–446, 1997.

[26] R. Rannacher and F.-T. Suttmeier. A posteriori error control in finite element methods via duality techniques: Application to perfect plasticity. *Computational Mechanics*, 21(2):123–133, 1998.

[27] R. Rannacher and F.-T. Suttmeier. A posteriori error estimation and mesh adaptation for finite element models in elasto-plasticity. *Computer Methods in Applied Mechanics and Engineering*, 176(14):333 – 361, 1999.

[28] F.-T. Suttmeier. On plasticity with hardening: Adaptive finite element discretization. *International Mathematical Forum*, 52:2591 – 2601, 2010.

[29] S.Sh. Ghorashi, T. Lahmer, A.S. Bagherzadeh, and T. Rabczuk. Goal-oriented error estimation and mesh adaptivity in elasticity problems with heterogeneous material distribution. submitted.

[30] S.Sh. Ghorashi, J. Amani, A.S. Bagherzadeh, and T. Rabczuk. Goal-oriented error estimation and mesh adaptivity in three-dimensional elasticity problems. *WCCM XI- ECCM V - ECFD VI, Barcelona, Spain*, 2014.

[31] W. Bangerth, R. Hartmann, and G. Kanschat. Deal.ii—a general-purpose object-oriented finite element library. *ACM Transactions on Mathematical Software (TOMS)*, 33(4), August 2007.

[32] W. Bangerth, T. Heister, L. Heltai, G. Kanschat, M. Kronbichler, M. Maier, B. Turcksin, and T. D. Young. The `deal.II` library, version 8.2. *Archive of Numerical Software*, 3, 2015.

[33] C. Chen and O.L. Mangasarian. Smoothing methods for convex inequalities and linear complementarity problems. *Mathematical Programming*, 71(1): 51–69, 1995.

[34] P. Areias and T. Rabczuk. Smooth finite strain plasticity with non-local pressure support. *International Journal for Numerical Methods in Engineering*, 81(1):106–134, 2010.

[35] P. Areias and T. Rabczuk. Finite strain fracture of plates and shells with configurational forces and edge rotations. *International Journal for Numerical Methods in Engineering*, 94(12):1099–1122, 2013.

[36] J. Frohne, T. Heister, and W. Bangerth. Efficient numerical methods for the large-scale, parallel solution of elastoplastic contact problems. *International Journal for Numerical Methods in Engineering*, 105(6):416–439, 2016.

[37] J.C. Simo and T.J.R. Hughes. *Computational inelasticity*. Springer, 1998.

[38] M. Sauter and C. Wieners. On the superlinear convergence in computational elasto-plasticity. *Computer Methods in Applied Mechanics and Engineering*, 200(49–52):3646–3658, 2011.

[39] P. Ladevéze and L. Chamoin. Calculation of strict error bounds for finite element approximations of non-linear pointwise quantities of interest. *International Journal for Numerical Methods in Engineering*, 84(13):1638–1664, 2010.

[40] P.R. Budarapu, R. Gracie, S.W. Yang, X. Zhaung, and T. Rabczuk. Efficient coarse graining in multiscale modeling of fracture. *Theoretical and Applied Fracture Mechanics*, 69:126–143, 2014.

[41] P.R. Budarapu, R. Gracie, S.P.A. Bordas, and T. Rabczuk. An adaptive multiscale method for quasi-static crack growth. *Computational Mechanics*, 53(6):1129–1148, 2014.

[42] S.W. Yang, P.R. Budarapu, D.R. Mahapatra, S.P.A. Bordas, G. Zi, and T. Rabczuk. A meshless adaptive multiscale method for fracture. *Computational Materials Science*, 96:382–395, 2015.

[43] D. W. Kelly, J. P. De S. R. Gago, O. C. Zienkiewicz, and I. Babuška. A posteriori error analysis and adaptive processes in the finite element method: Part i error analysis. *International Journal for Numerical Methods in Engineering*, 19(11):1593–1619, 1983.

[44] X.-L. Gao. Elasto-plastic analysis of an internally pressurized thick-walled cylinder using a strain gradient plasticity theory. *International Journal of Solids and Structures*, 40(23):6445 – 6455, 2003.

[45] P.S. Theocaris and E. Marketos. Elastic-plastic analysis of perforated thin strips of a strain-hardening material. *Journal of the Mechanics and Physics of Solids*, 12(6):377 – 380, 1964.